



Graphene oxide-induced synthesis of button-shaped amorphous Fe₂O₃/rGO/CNFs films as flexible anode for high-performance lithium-ion batteries

Qingshan Zhao^a, Jialiang Liu^a, Xinxin Li^a, Zhengzheng Xia^a, Qixia Zhang^a, Min Zhou^b, Wei Tian^a, Ming Wang^a, Han Hu^a, Zhongtao Li^a, Wenting Wu^a, Hui Ning^a, Mingbo Wu^{a,*}

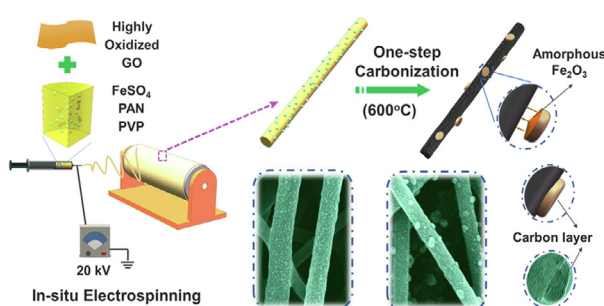
^a State Key Laboratory of Heavy Oil Processing, Institute of New Energy, College of Chemical Engineering, China University of Petroleum (East China), Qingdao 266580, China

^b Beijing Lehua Lithium Energy Science and Technology Ltd., Beijing 100193, China

HIGHLIGHTS

- Graphene oxide induces synthesis of button-shaped amorphous Fe₂O₃/rGO/CNFs films.
- The am-Fe₂O₃/rGO/CNFs shows a capacity of 584 mA h g⁻¹ at 2 A g⁻¹ after 400 cycles.
- The film exhibits good flexibility and can be utilized as flexible anodes for LIBs.
- The hierarchical structure accounts for the excellent electrochemical performance.

GRAPHICAL ABSTRACT



ARTICLE INFO

Keywords:

Amorphous Fe₂O₃
Graphene oxide
Carbon nanofibers
Flexible electrode
Lithium-ion batteries

ABSTRACT

Constructing high-performance flexible lithium-ion batteries (LIBs) is imperative to satisfy the rapid demand of flexible and wearable electronics. Herein, we demonstrate a novel strategy to fabricate button-shaped amorphous Fe₂O₃/rGO/carbon nanofibers (am-Fe₂O₃/rGO/CNFs) films as freestanding flexible anodes for LIBs through in-situ electrospinning and subsequent one-step carbonization. Intercalating highly oxidized GO into the electrospun precursor not only induces tight growth of button-shaped amorphous Fe₂O₃ nanoparticles onto rimous CNFs matrix, but also substantially enhances the mechanical flexibility of the resulting films. Owing to the distinctive hierarchical structure, especially amorphous nature of Fe₂O₃ and intimate connection between am-Fe₂O₃ and the conductive substrate, the am-Fe₂O₃/rGO/CNFs-20 film delivers an excellent reversible capacity of 811 mA h g⁻¹ at 0.1 A g⁻¹, as well as remarkable rate performance and cycling stability (584 mA h g⁻¹ over 400 cycles at a high current density of 2 A g⁻¹). The electrode also exhibits impressive flexibility, which can power an array of light-emitting diodes, even bended and folded, demonstrating great potential for flexible LIBs. The facile synthesis strategy and excellent electrochemical performance endow it with great potential for application in flexible energy storage.

1. Introduction

With the rapid development of flexible electronic devices and

wearable electronics, great efforts have been devoted to fabricating flexible power sources [1]. Among the various energy storage technologies, rechargeable lithium-ion batteries (LIBs) stand out due to

* Corresponding author.

E-mail address: wumb@upc.edu.cn (M. Wu).

<https://doi.org/10.1016/j.cej.2019.03.076>

Received 22 December 2018; Received in revised form 24 February 2019; Accepted 8 March 2019

Available online 09 March 2019

1385-8947/© 2019 Published by Elsevier B.V.

their high energy density, appropriate operating voltage, relatively low self-discharge, and long lifespan [2]. So high-energy flexible LIBs have drawn considerable attention in recent years [3–5]. Generally, the performance of LIBs greatly depends on the electrodes, especially the anode materials [6–8]. Therefore, flexible anodes with satisfactory electrochemical performance and robust mechanical flexibility are the focus of scientific interests.

Owing to the good lithium storage performance, excellent conductivity, and favorable flexibility, self-supporting carbon nanomaterials (CNMs) such as carbon nanofibers (CNFs), carbon nanowires, graphene etc. show great potential as promising flexible anode materials [9–12]. Their unique nanostructures make it easy to be assembled or pressed into thin films or papers, which can be directly utilized as flexible freestanding electrodes without any binder or conductive additive. Considering the limited energy density, coupling with other active materials provides an efficient approach to improve the reversible capacity of carbon nanomaterials [13–15]. Nanostructured transition metal oxides (TMOs) are emerging as alternative anodes due to their high theoretical capacities, which yet suffers from low conductivity and poor cycling stability [16,17]. Therefore, TMOs/CNMs composites have been extensively investigated to combine their individual advantages together [18–20]. Even so, to satisfy the future demands for large energy and power densities, flexible anodes with high reversible capacity and long cycle stability, as well as excellent rate capability, still remain a big challenge [21].

Recently, there is growing interest in the application of amorphous TMOs (am-TMOs) in LIBs because of their unique electrochemical behavior [22–24]. First-principles calculations reveal lower Gibbs free energy change of am-TMOs than their crystalline counterparts, implying superior reversibility of the conversion reaction in charge/discharge processes [25]. The amorphous nature allows absence of lattice boundaries in internal space, which facilitates the percolation and diffusion of Li^+ ions and leads to promoted rate capability. Consequently, am-TMOs/CNMs composites were designed and reported as dominant anodes for LIBs and flexible LIBs [26–28]. For instance, Wang et al. sulfurized MoO_x /ethylenediamine nanowire to synthesize amorphous $\text{MoS}_2/\text{MoO}_3$ on nitrogen-doped carbon nanowires, which showed a reversible capacity of $887.5 \text{ mA h g}^{-1}$ at 1 A g^{-1} after 350 cycles [29]. Shiratori et al. decorated amorphous Fe_2O_3 on electrospun CNFs through electrodeposition and subsequent thermal annealing (300°C). The resulting self-supporting $\text{Fe}_2\text{O}_3/\text{CNFs}$ presented a capacity of 518 mA h g^{-1} at 0.05 A g^{-1} [30]. To synthesize and anchor am-TMOs active species on CNMs, low-temperature conversion/calcination, hydrothermal etc. methods have been employed. Nevertheless, the mild synthesis conditions would cause incompact connection between am-TMOs and the carbon skeletons, resulting in inferior electrochemical performance. More importantly, many am-TMOs/CNMs composites showed even poor flexibility, which seriously restricts their application in flexible LIBs. Therefore, developing feasible methods to synthesize advanced am-TMOs/CNMs flexible electrodes for LIBs is urgently needed.

Herein, we demonstrate a novel and facile approach to fabricate amorphous $\text{Fe}_2\text{O}_3/\text{rGO}$ /carbon nanofibers (am- $\text{Fe}_2\text{O}_3/\text{rGO}/\text{CNFs}$) films as flexible and freestanding anodes for LIBs. By employing FeSO_4 , graphene oxide (GO), polyacrylonitrile (PAN), and polyvinylpyrrolidone (PVP) as precursors, am- $\text{Fe}_2\text{O}_3/\text{rGO}/\text{CNFs}$ films are synthesized via in-situ electrospinning and subsequent one-step carbonization at 600°C . With abundant oxygen functional groups, the intercalated GO unexpectedly induces tight growth of button-shaped amorphous Fe_2O_3 (am- Fe_2O_3) nanoparticles onto rimous CNFs, which is well-coated by a thin layer of carbon. Simultaneously, GO is reduced to rGO and embedded into the nanofibers, substantially enhancing the mechanical flexibility of the electrodes. Owing to the distinctive hierarchical structure, the resulting am- $\text{Fe}_2\text{O}_3/\text{rGO}/\text{CNFs}$ composites are evaluated as high-performance freestanding anodes for LIBs. Especially, the am- $\text{Fe}_2\text{O}_3/\text{rGO}/\text{CNFs}$ -20 film delivers an excellent reversible

capacity of 811 mA h g^{-1} at 0.1 A g^{-1} , as well as remarkable rate performance and cycling stability (584 mA h g^{-1} over 400 cycles at a high current density of 2 A g^{-1}). The excellent mechanical flexibility of the film also demonstrates great potential for application in flexible LIBs.

2. Experimental section

2.1. Preparation of am- $\text{Fe}_2\text{O}_3/\text{rGO}/\text{CNFs}$

All reagents were of analytical grade and used without further purification. Highly oxidized GO was synthesized through an improved mixed acid method [31]. Briefly, 3.0 g graphite flakes and 18.0 g KMnO_4 were added into a concentrated $\text{H}_2\text{SO}_4/\text{H}_3\text{PO}_4$ (360:40 mL) solution, which was heated to 50°C and stirred for 12 h. The mixture was cooled to room temperature with 400 mL ice water containing 3 mL H_2O_2 (30%). After filtered through polyester fiber, the filtrate was centrifuged at 4000 rpm for 4 h. The remaining solid was then filtered and washed in succession with 5% aqueous HCl and deionized water. The GO product was further purified by dialysis for three days.

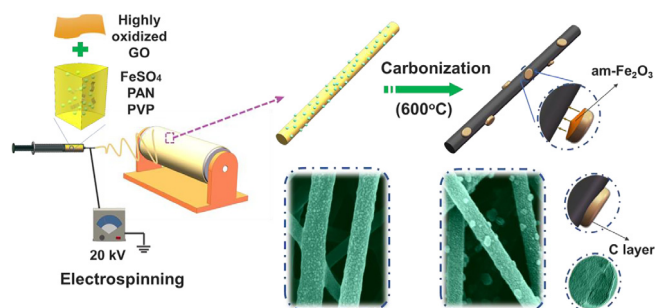
In a typical synthesis procedure of am- $\text{Fe}_2\text{O}_3/\text{rGO}/\text{CNFs}$, 4 equivalent $\text{FeSO}_4 \cdot 7\text{H}_2\text{O}$ and certain GO powder was added into 20 mL N, N-dimethylformamide (DMF), followed by stirring and ultrasonication for 1.0 h (25 W, 40 kHz). 1 g PAN and 1 g PVP were poured into the mixture and vigorously stirred to get a homogeneous precursor solution for electrospinning. Subsequently, the solution was injected into a plastic injector with a 19G needle of 1.1 mm inner diameter and electrospun on a spinning machine at a voltage of 20 kV. The propelling rate of the injector was set as $2 \mu\text{m s}^{-1}$. The distance between spinning needle and cylinder (rotary speed 400 r min^{-1}) was 16 cm to collect the nanofibers and obtain an as-spun film ($\text{FeSO}_4/\text{GO}/\text{PAN}/\text{PVP}$), which was directly carbonized at 600°C for 2 h under a heating rate of 3°C min^{-1} in nitrogen atmosphere. The resulting flexible film was denoted as am- $\text{Fe}_2\text{O}_3/\text{rGO}/\text{CNFs}$. To optimize the GO addition amount, am- $\text{Fe}_2\text{O}_3/\text{rGO}/\text{CNFs}$ films with 10 mg, 20 mg, and 50 mg GO amount were prepared and denoted as am- $\text{Fe}_2\text{O}_3/\text{rGO}/\text{CNFs}$ -10, am- $\text{Fe}_2\text{O}_3/\text{rGO}/\text{CNFs}$ -20, and am- $\text{Fe}_2\text{O}_3/\text{rGO}/\text{CNFs}$ -50, respectively. As a control, FeO_x/CNFs -0 was synthesized under the same experimental conditions except for adding GO. To investigate the state of rGO, rGO/CNFs-20 was also prepared without adding $\text{FeSO}_4 \cdot 7\text{H}_2\text{O}$ into the precursor solution.

2.2. Characterization

Scanning electron microscopy (SEM) images and line-scan energy dispersive X-ray spectroscopy (EDS) were recorded on a Hitachi S-4800 instrument. Transmission electron microscopy (TEM) images and energy dispersive X-Ray spectroscopy (EDX) were recorded on a JEM-2100 microscope operating at 200 kV. The tensile test was performed on a mechanical testing machine (HY0580, Shanghai Hengyi Testing Machine Company, China). The crystal structure was characterized with X-ray diffraction (XRD) (X'Pert PRO MPD, Holland) using Cu K α radiation ($k = 1.518 \text{ \AA}$) in angle of 2 theta from 5° to 70° . Raman spectroscopy was collected using a LabRAM HR Evolution (France). The Mössbauer spectrum was provided with a ^{57}Co (Pd) source at room temperature with a Wissel electromechanical spectrometer. X-ray photoelectron spectroscopy (XPS) analysis was conducted using an Mg K α (1486.6 eV) monochromatic X-ray source (Escalab 250Xi, Thermo Scientific). Thermal gravimetric analysis (TGA) was conducted in air at a heating rate of 5°C min^{-1} (STA 409 PC Luxx, Germany).

2.3. Electrochemical measurements

The electrochemical performance of the as-prepared am- $\text{Fe}_2\text{O}_3/\text{rGO}/\text{CNFs}$ films were examined using CR2032-type coin cells at room temperature. The films were directly cut into working electrodes (11 mm in diameter) and assembled in the cells in an Ar-filled glove box



Scheme 1. Illustration for the synthesis of am-Fe₂O₃/rGO/CNFs films.

(O₂ < 0.1 ppm and H₂O < 0.1 ppm) with lithium metal as counter electrode. Binders, conductive agents and current collector are not necessary. The mass loading of am-Fe₂O₃/rGO/CNFs anodes are 1.5–2.0 mg·cm⁻². Celgard 2300 membrane was utilized as the separator, and the electrolyte comprised 1 M LiPF₆ in a 1:1 (v/v) mixture of ethylene carbonate and dimethyl carbonate (EC/DMC). The discharge and charge processes were tested on a LAND CT2001A battery test system over a voltage range of 0.01–3.00 V vs. Li/Li⁺. The electrochemical impedance spectroscopy (EIS) tests were performed at a frequency range of 100 KHz–10 MHz with an AC voltage amplitude of 5 mV on an Ametek PARSTAT4000 electrochemistry workstation.

3. Results and discussion

The am-Fe₂O₃/rGO/CNFs films were synthesized by a facile method as illustrated in Scheme 1. Serving as an additive agent and iron resource, respectively, GO and FeSO₄ were added into the PAN and PVP precursor solution. GO with abundant oxygen-containing groups shows strong coordination interactions with metal ions [32]. So the Fe²⁺ precursors were adsorbed onto GO surface and buried into the as-spun nanofibers through an in-situ electrospinning procedure. Flexible am-Fe₂O₃/rGO/CNFs films were further obtained via subsequent one-step carbonization. In this stage, the strong anchoring interaction and spatial hindrance effect induced by two-dimensional GO/rGO nanosheets restrict the migration of iron species [33]. The different migration rate results in formation of small amorphous Fe₂O₃ clusters or nanoparticles at the nucleation sites, followed by coalescence via solid state diffusion, resulting in button-shaped am-Fe₂O₃ nanoparticles. Covered by a thin carbon layer, the am-Fe₂O₃ nanoparticles were tightly anchored onto the surface of rimous CNFs matrix. With the assistance of GO, flexible am-Fe₂O₃/rGO/CNFs films were readily prepared and could be utilized as freestanding anode materials for LIBs.

SEM images of the samples with different addition amount of GO are shown in Fig. 1 a–d. FeO_x/CNFs-0 composite, that means, none GO is added, exhibits big nanoparticles with non-uniform sizes located on discontinuous nanofibers (Fig. 1a). The fractured feature should be caused by excess iron salt, leading to poor spinnability and bad flexibility of the resulting film (Fig. S1). As a contrast, am-Fe₂O₃/rGO/CNFs-10, am-Fe₂O₃/rGO/CNFs-20, and am-Fe₂O₃/rGO/CNFs-50 all exhibit continuous nanofibers. Since no GO nanosheets can be observed between or around the nanofibers, rGO/CNFs-20 (to exclude the influence of iron oxides) was prepared and characterized to elucidate this phenomenon (Fig. S2). The SEM and TEM images reveal GO nanosheets are broken into fragments in the electrospinning process and embedded into the nanofibers, acting as cross-linking networks to substantially improve the flexibility of the resulting film [34]. The addition amount of GO greatly affects the morphology and structure of the samples. When small amount of GO is incorporated, the hindrance effect of GO is weak, resulting in more nucleation and growth sites for iron precursors. Small nanoparticles with uniform distribution are generated on the surface and inner of CNFs for am-Fe₂O₃/rGO/CNFs-10 (Fig. 1b). As to am-Fe₂O₃/rGO/CNFs-20, enhanced hindrance effect induced by GO

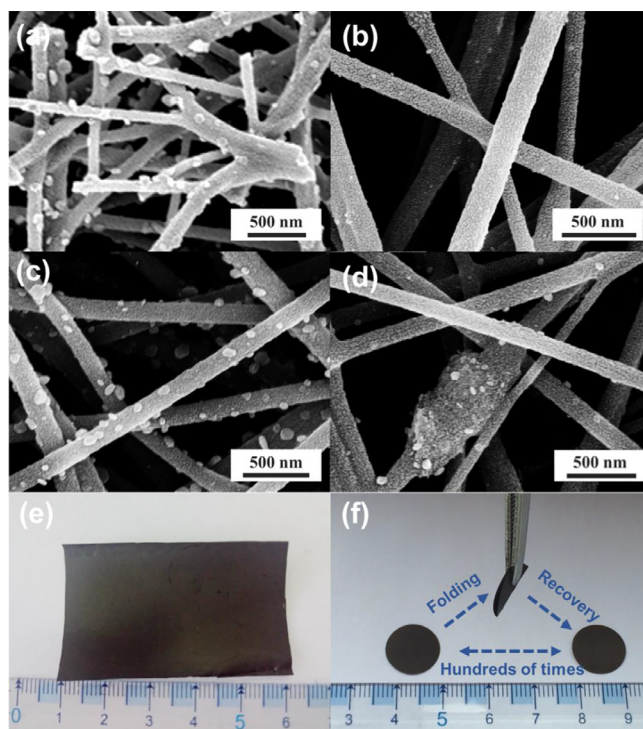


Fig. 1. SEM images of the FeO_x/CNFs-0 (a), am-Fe₂O₃/rGO/CNFs-10 (b), am-Fe₂O₃/rGO/CNFs-20 (c), and am-Fe₂O₃/rGO/CNFs-50 (d). Digital photograph of am-Fe₂O₃/rGO/CNFs-20 film (e) and its flexible test (f).

would lead to less nucleation and growth sites, achieving button-shaped nanoparticles with larger size and uniform distribution (Fig. 1c). However, excess GO causes agglomeration and formation of protuberances in the am-Fe₂O₃/rGO/CNFs-50 nanofibers (Fig. 1d). As a result, abundant nanoparticles are generated and distributed on the protuberances. As shown in Fig. 1e–f, the as-prepared flexible am-Fe₂O₃/rGO/CNFs-20 film can be directly tailored into freestanding working electrodes, which can be repeatedly folded for hundreds of times and preserve their initial configuration. Tensile test was performed on am-Fe₂O₃/rGO/CNFs-20, and it shows a tensile strength of 1.06 Mpa, further revealing its good mechanical property.

Raman spectra were conducted to investigate the structural change induced by GO. Fig. 2a illustrates the presence of two characteristic

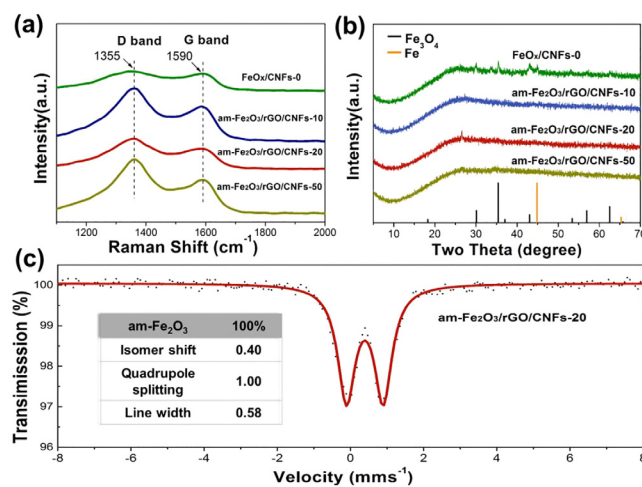


Fig. 2. Raman spectra (a) and XRD patterns (b) of FeO_x/CNFs-0, am-Fe₂O₃/rGO/CNFs-10, am-Fe₂O₃/rGO/CNFs-20, and am-Fe₂O₃/rGO/CNFs-50. RT Mössbauer spectrum of am-Fe₂O₃/rGO/CNFs-20 (c).

bands at around 1355 and 1590 cm^{-1} , corresponding to D band (disordered structure) and G band (graphitic structure), respectively [35]. Compared with $\text{FeO}_x/\text{CNFs-0}$, incorporation of GO results in enhanced disorder and obvious increases of intensity ratio (I_D/I_G) from 1.13 to 1.53, 1.59, and 1.61, respectively. The similar I_D/I_G value of am- $\text{Fe}_2\text{O}_3/\text{rGO}/\text{CNFs-10}$, am- $\text{Fe}_2\text{O}_3/\text{rGO}/\text{CNFs-20}$, and am- $\text{Fe}_2\text{O}_3/\text{rGO}/\text{CNFs-50}$ would provide more evidence for the embedment of GO fragments in the nanofibers. As seen in Fig. 2b, XRD pattern of $\text{FeO}_x/\text{CNFs-0}$ shows diffraction peaks assigned to magnetite Fe_3O_4 (JCPDS: 85-1436) and elemental Fe (JCPDS: 87-0722), arising from the thermal reduction effect during the pyrolysis process. Interestingly, with the existence of GO, no diffraction peaks of crystalline FeO_x can be observed in the XRD patterns of am- $\text{Fe}_2\text{O}_3/\text{rGO}/\text{CNFs-10}$, am- $\text{Fe}_2\text{O}_3/\text{rGO}/\text{CNFs-20}$, and am- $\text{Fe}_2\text{O}_3/\text{rGO}/\text{CNFs-50}$, indicating their amorphous nature with no contribution from crystalline phase. It should be noted that the small sharp peak at around 26.5° should be ascribed to partial crystallization of $\alpha\text{-Fe}_2\text{O}_3$ (JCPDS no. 47-1409) or signal interference. Consequently, room temperature (RT) ^{57}Fe Mössbauer spectroscopy was measured to determine chemical components of the nanoparticles. The spectrum of am- $\text{Fe}_2\text{O}_3/\text{rGO}/\text{CNFs-20}$ shows a well-defined single quadrupole split doublet of non-Lorentzian shape, arising from the electric field gradient distribution encountered in amorphous iron (III) oxides [36]. The isomer shift ($\delta = 0.40 \text{ mm s}^{-1}$) and spectral line width ($\Gamma_{1/2} = 0.58 \text{ mm s}^{-1}$) correspond to high-spin Fe^{3+} ions in octahedral coordination [37]. The quadrupole splitting value ($\Delta E_Q = 1.00 \text{ mm s}^{-1}$) is relatively higher than other amorphous Fe_2O_3 samples, reflecting a large distortion of the octahedral environment of Fe nuclei, which just inosculates with their special button-shaped morphology. The above results verify the significant role of GO on the composite structure and mechanical flexibility of the am- $\text{Fe}_2\text{O}_3/\text{rGO}/\text{CNFs}$ films, which can be regulated by varying the GO addition amount. Intercalating highly oxidized GO into the electrospun precursor not only induces the synthesis of amorphous Fe_2O_3 nanoparticles, but also substantially enhances the mechanical flexibility of the resulting films. Among them, am- $\text{Fe}_2\text{O}_3/\text{rGO}/\text{CNFs-20}$ displays the optimized ratio and best characteristics for flexible lithium storage applications.

Considering the best characteristics and great potential as flexible electrodes, the nanostructure and properties of am- $\text{Fe}_2\text{O}_3/\text{rGO}/\text{CNFs-20}$ were detailedly studied. As shown in Fig. 3, SEM and TEM images show that plenty button-shaped am- Fe_2O_3 nanoparticles are well-distributed onto the nanofibers with a uniform diameter around 140 nm. The rimous nanofibers with abundant cracks would be beneficial for the complete wetting of the electrolyte and provide ideal channels for Li^+ ions diffusion and accessible lithium storage sites [38]. According to the high-resolution TEM images, button-shaped Fe_2O_3 nanoparticles can be clearly distinguished, verifying the amorphous nature of Fe_2O_3 for none lattice fringes being observed (Fig. 3c–d). The bottom-up grown am- Fe_2O_3 nanoparticles are intimately attached onto the surface of CNFs matrix. It worth mentioning that their connection is strengthened with the coated thin carbon layer ($\sim 2.7 \text{ nm}$) over the am- Fe_2O_3 nanoparticles. Such special core–shell structure would greatly reinforce their connection and stability in the charge–discharge processes [39]. The TEM images also reveals the well presence of two-dimensional rGO nanosheets embedded into the nanofibers, in accordance with the above result (Fig. S3). EDX mapping of am- $\text{Fe}_2\text{O}_3/\text{rGO}/\text{CNFs-20}$ displays the presence of C, N, O, and Fe elements and evidences the well-defined distribution of am- Fe_2O_3 on the nanofibers (Fig. 3e). The doped-nitrogen should derive from PAN, which is beneficial to improve the conductivity of CNFs. The result is completely consistent with the EDS line-scan pattern, confirming the excellent distribution and desirable deposition of am- Fe_2O_3 nanoparticles (Fig. S4).

Fig. S5 shows the XPS analysis results of am- $\text{Fe}_2\text{O}_3/\text{rGO}/\text{CNFs-20}$. In accordance with EDX results above, the full-range XPS spectrum presents C, N, O, and Fe peaks. High-resolution Fe 2p XPS spectrum shows $\text{Fe } 2p_{3/2}$ and $\text{Fe } 2p_{1/2}$ peaks at 710.4 and 724.0 eV, respectively, with a satellite peak at 718.2 eV, corresponding to the binding energy of Fe^{3+}

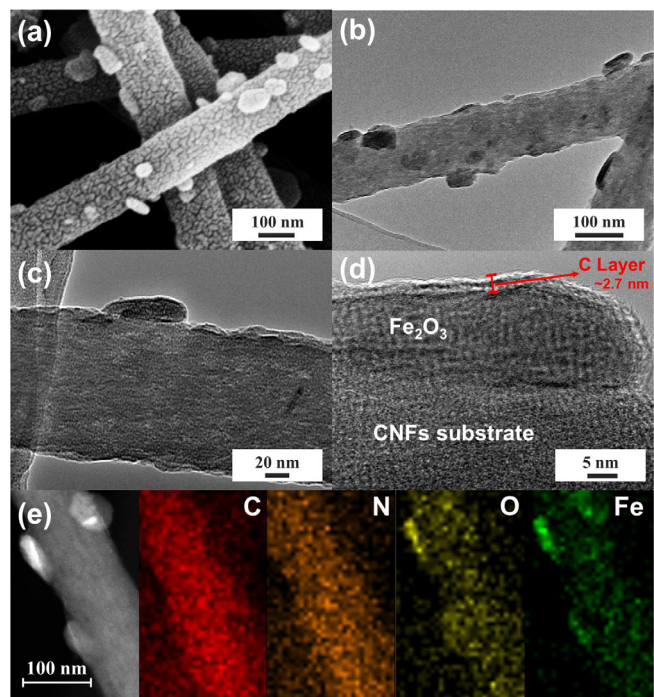


Fig. 3. SEM image (a) and TEM images of am- $\text{Fe}_2\text{O}_3/\text{rGO}/\text{CNFs-20}$ at different magnifications (b–d). TEM image and corresponding EDX elemental mappings of C, N, O, and Fe, respectively (e).

ions [40]. Notably, in comparison with C1s XPS spectrum of GO, am- $\text{Fe}_2\text{O}_3/\text{rGO}/\text{CNFs-20}$ displays a significant decrease in the C–O peak, suggesting the deoxygenation of GO to rGO in the thermal treatment process [41]. Thus, the buried rGO fragments not only serves as cross-linking networks to improve the spinnability and flexibility, but also provides enhanced conductive channels for electron transport along the nanofibers. O 1s XPS spectrum of am- $\text{Fe}_2\text{O}_3/\text{rGO}/\text{CNFs-20}$ can be divided into three peaks at 532.8, 531.5, and 530.5 eV, corresponding to the binding energy of C–O, Fe–O–C, and Fe–O, respectively [42]. The dominant Fe–O–C peak reveals strong chemical bonding between the carbonaceous substrate and Fe_2O_3 [43]. Such strong interaction would be beneficial to the fast electron transfer and buffer the expansion of Fe_2O_3 , leading to improved electrochemical properties. Thermal gravimetric analysis (TGA) was conducted in air at a heating rate of $5^\circ \text{C min}^{-1}$ to evaluate the Fe_2O_3 content (Fig. S6). The sample starts to lose weight along with temperature rises. The main weight loss between 300°C and 500°C is mainly ascribed to carbon pyrolysis of CNFs and rGO. Only Fe_2O_3 was left after heating to 800°C , and the mass percentage of Fe_2O_3 is calculated to be 19.5 wt% in am- $\text{Fe}_2\text{O}_3/\text{rGO}/\text{CNFs-20}$.

The obtained am- $\text{Fe}_2\text{O}_3/\text{rGO}/\text{CNFs}$ composites are flexible free-standing films and can be directly utilized as anodes for LIBs without any binder, conductive agent or current collector. Coin cells were made to evaluate the electrochemical properties of the samples. Cyclic performance of $\text{FeO}_x/\text{CNFs-0}$, am- $\text{Fe}_2\text{O}_3/\text{rGO}/\text{CNFs-10}$, am- $\text{Fe}_2\text{O}_3/\text{rGO}/\text{CNFs-20}$, and am- $\text{Fe}_2\text{O}_3/\text{rGO}/\text{CNFs-50}$ were firstly compared at a current density of 1 A g^{-1} (Fig. 4a). All the composites show a sharp capacity decrease in the first few circles, followed by gradual increasing of the capacity, which is common for TMO-based electrodes [44,45]. The initial drops is generally caused by decomposition of electrolyte and formation of solid electrolyte interphase (SEI) film, while the following rise is generally attributed to electrochemical activation and reversible growth of a polymeric gel-like SEI film on the surface of the progressively pulverized particles resulting from electrochemical grinding effect [46]. Due to the existence of FeO_x active species (especially Fe_3O_4), $\text{FeO}_x/\text{CNFs-0}$ displays a relatively stable cyclic performance and

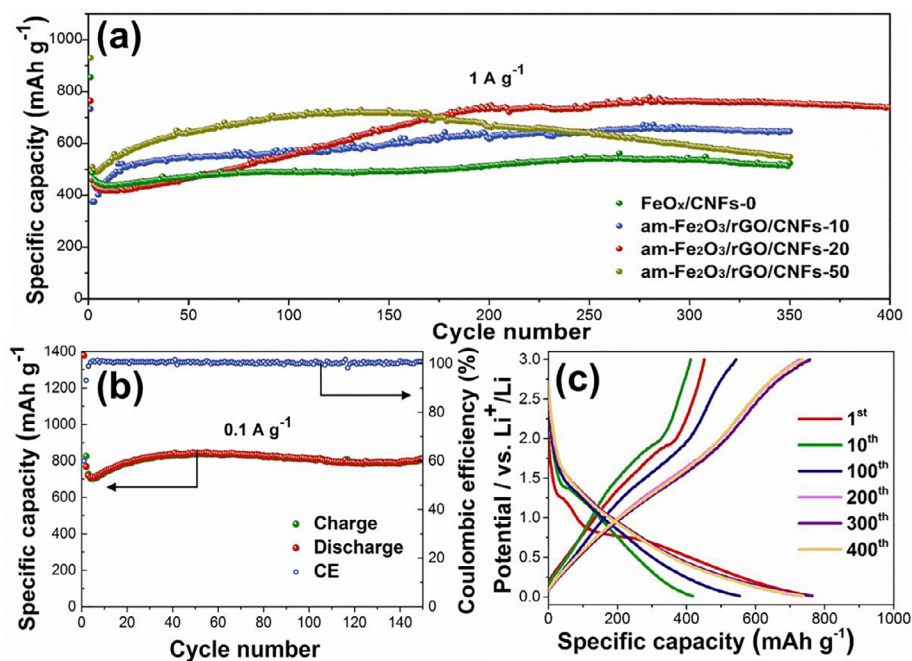


Fig. 4. Performance comparison of FeO_x/CNFs-0, am-Fe₂O₃/rGO/CNFs-10, am-Fe₂O₃/rGO/CNFs-20, and am-Fe₂O₃/rGO/CNFs-50 at 1 A g⁻¹ (a). Cyclic performance and corresponding CE of am-Fe₂O₃/rGO/CNFs-20 at 0.1 A g⁻¹ (b). Charge/discharge voltage profiles of am-Fe₂O₃/rGO/CNFs-20 (c).

presents a discharge capacity of 524 mA h g⁻¹ over 350 cycles [47]. Comparably, the smaller size and uniform distribution of amorphous Fe₂O₃ in am-Fe₂O₃/rGO/CNFs-10 avoids serious nanoparticle pulverization and thus leads in a sluggish capacity rise, affording an enhanced capacity of 646 mA h g⁻¹ after 350 cycles. Due to the larger nanoparticle size, am-Fe₂O₃/rGO/CNFs-20 involves in electrochemical activation and reversible growth of a polymeric gel-like film on the pulverized nanoparticles in the charge/discharge processes. The sample delivers an obvious rise and finally reaches a high reversible capacity of 739 mA h g⁻¹ over 400 cycles. While am-Fe₂O₃/rGO/CNFs-50 displays unstable performance, the capacity of which decreases from 714 mA h g⁻¹ to 548 mA h g⁻¹ after 350 cycles because of its unstable protuberance structure. Therefore, intercalation of GO can alter the composite characteristics, which further influence their electrochemical properties. As expected, am-Fe₂O₃/rGO/CNFs-20 achieves the best electrochemical performance. Cyclic performance of am-Fe₂O₃/rGO/CNFs-20 at 0.1 A g⁻¹ was further determined (Fig. 4b). The sample delivers a discharge and charge capacity of 1378 and 825 mA h g⁻¹ in the first cycle, respectively, with a coulombic efficiency (CE) of 60.0%. The relatively low CE is mainly caused by the irreversible formation of SEI film, as well as the abundant active sites on CNFs to cause decomposition of the electrolyte [48,49]. Whereafter, the electrode shows a stable reversible capacity and finally affords 811 mA h g⁻¹ after 150 cycles, with CE maintained steadily around 100%.

To fully uncover the electrochemical mechanism, galvanostatic discharge–charge profiles of am-Fe₂O₃/rGO/CNFs-20 were performed in 0.01–3.0 V voltage range at 1 A g⁻¹ (Fig. 4c). In the first discharge process, the inclined slope between 1.4 and 0.8 V and voltage plateaus at 0.7 V reveals the reduction of Fe³⁺ to Fe²⁺ and Fe²⁺ to Fe⁰, respectively [50]. The long slope below 0.7 V should mainly originate from the Li⁺ ions storage in CNFs. Correspondingly, in the charge curve, the sloped region from 0.8 to 1.9 V is attributed to the reverse oxidation reaction of Fe⁰ to Fe³⁺ [40,51]. In line with the cyclic performance, the electrode shows a capacity loss in the first few cycles, followed by a gradual upswing. The capacity stabilizes at around 734 mA h g⁻¹ in the 200th cycle, with a CE approaching 100%. The discharge and charge curves almost overlap in the following 300th and 400th cycle, implying the sustained excellent reversibility of the

conversion mechanism in the anode. Remarkably, with the increase of recycling time, the voltage hysteresis becomes much narrower as confirmed by the closer discharge/charge voltage profiles, suggesting faster reaction kinetics of the electrode owing to the amorphous nature of Fe₂O₃ [52–54].

Fig. 5a presents a robust and stable rate performance of am-Fe₂O₃/rGO/CNFs-20 at different current densities ranging from 0.1 to 2 A g⁻¹. After 100 cycles at a current density of 2 A g⁻¹, am-Fe₂O₃/rGO/CNFs-20 delivers a specific capacity of 889 mA h g⁻¹ at 0.1 A g⁻¹. When the current density is changed to 0.2, 0.5, 1, and 2 A g⁻¹, the electrode presents high capacities of 819, 738, 664, and 570 mA h g⁻¹, respectively. As the current density is recovered to 0.1 A g⁻¹, a reversible capacity of 875 mA h g⁻¹ is achieved. Considering the great potential for LIBs with high energy and power densities, its long-term cyclic performance was subsequently conducted at a high current density of 2 A g⁻¹ (Fig. 5b). After a sharp decrease in the first few cycles, the capacity goes up and shows a long stable reversible capacity about 580 mA h g⁻¹ in the following cycles (CE around 100%), and finally affords a satisfactory capacity of 584 after 400 cycles. Table 1S shows the electrochemical performance of Fe₂O₃-based anode materials reported in recent literatures. One can find that the am-Fe₂O₃/rGO/CNFs-20 displays comparable or superior performance to previous studies. Especially, as a flexible electrode, the composite shows excellent reversible capacities and good stability at high current densities. As a further proof of concept, the am-Fe₂O₃/rGO/CNFs-20 film was also cut into rectangle pieces and assembled into a flexible LIBs. As shown in Fig. 5c-f, the flat packaged battery can power an array of commercial colored light-emitting diodes (LEDs). Notably, the battery still works normally when it is bended and folded to different angles (around 45°, 90°, and 180°), demonstrating the excellent mechanical flexibility of am-Fe₂O₃/rGO/CNFs-20 electrode and its great potential for application in flexible energy storage devices.

In order to shed light on the superior electrochemical performance of the am-Fe₂O₃/rGO/CNFs electrodes, electrochemical impedance spectroscopy (EIS) measurements were recorded (Fig. 6a). The semi-circle at high-medium frequency is assigned to the charge-transfer resistance (R_c) and Li⁺ ions migration resistance through the SEI film (R_s). While the inclined line at low frequency is related to the Warburg

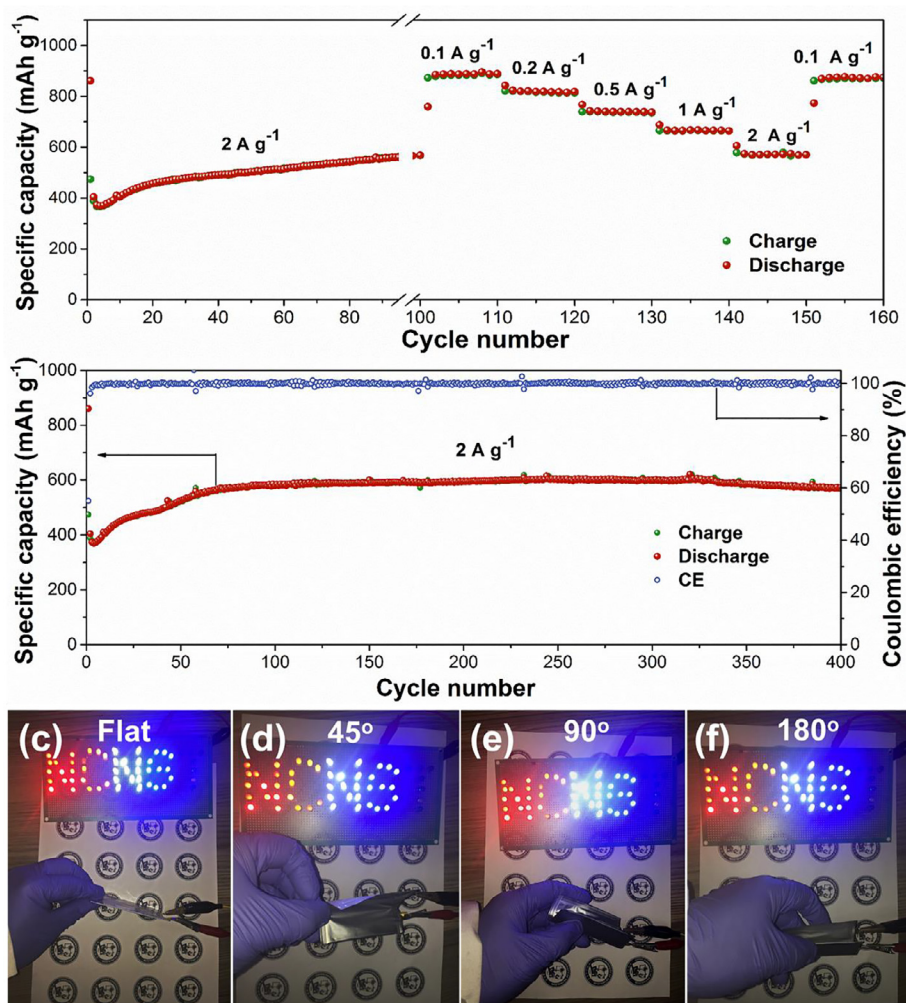


Fig. 5. Rate capability (a) and long-term cyclic capability at 2 A g^{-1} (b) of $\text{am-Fe}_2\text{O}_3/\text{rGO}/\text{CNFs-20}$. Photographs demonstration of the flexibility of the freestanding $\text{am-Fe}_2\text{O}_3/\text{rGO}/\text{CNFs-20}$ electrode by flat (c), and bended for 45° (d), 90° (e), and 180° (f), respectively.

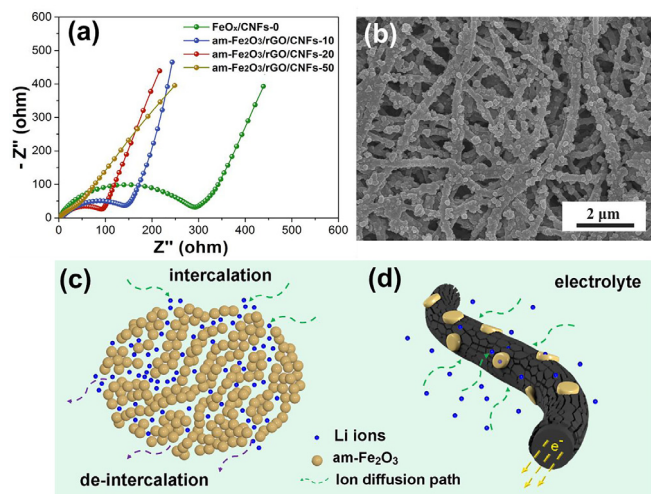


Fig. 6. Nyquist plots of $\text{FeO}_x/\text{CNFs-0}$, $\text{am-Fe}_2\text{O}_3/\text{rGO}/\text{CNFs-10}$, $\text{am-Fe}_2\text{O}_3/\text{rGO}/\text{CNFs-20}$, and $\text{am-Fe}_2\text{O}_3/\text{rGO}/\text{CNFs-50}$ (a). SEM image of $\text{am-Fe}_2\text{O}_3/\text{rGO}/\text{CNFs-20}$ after 400 cycles at 2 A g^{-1} (b). Schematic illustration diffusion paths of Li^+ ions into $\text{am-Fe}_2\text{O}_3$ (c) and the hierarchical microstructure of $\text{am-Fe}_2\text{O}_3/\text{rGO}/\text{CNFs}$ (d).

impedance (W_s), which is associated with the diffusion of Li^+ ions into the bulk electrodes [55,56]. Compared with $\text{FeO}_x/\text{CNFs-0}$, the

increasing amount of GO leads to obvious gradual decrease of the semicircle diameter, suggesting improved charge transfer and Li^+ ions diffusion kinetics. The strong interfacial interaction between conductive CNFs substrate and $\text{am-Fe}_2\text{O}_3$ guarantees the rapid charge transfer. The rimous CNFs with abundant cracks facilitate the complete wetting of the electrolyte, providing shorter and faster channels for Li^+ ions diffusion. However, as confirmed by the SEM results above, excess GO causes serious agglomeration in CNFs and leads to a quite low slope in the low frequency range for $\text{am-Fe}_2\text{O}_3/\text{rGO}/\text{CNFs-50}$. In comparison, $\text{am-Fe}_2\text{O}_3/\text{rGO}/\text{CNFs-10}$ and $\text{am-Fe}_2\text{O}_3/\text{rGO}/\text{CNFs-20}$ show much higher slope than $\text{FeO}_x/\text{CNFs-0}$, indicating higher Li^+ ions diffusion in the electrodes. The robust architectural stability of the electrode was further confirmed by the SEM result (Fig. 6b). Compared with Fig. 1c above, additional smaller nanoparticles are distributed on CNFs after 400 charge/discharge cycles at of 2 A g^{-1} , which should be ascribed to exposure of buried $\text{am-Fe}_2\text{O}_3$ to the surface, as well as partial pulverization of $\text{am-Fe}_2\text{O}_3$ through the electrochemical cycle processes. The whole composite is coated by a layer of SEI film on the surface. Still, the $\text{am-Fe}_2\text{O}_3/\text{rGO}/\text{CNFs-20}$ composite shows excellent stability and maintains its hierarchical structure.

On account of the above results, the superior lithium-ion storage properties of $\text{am-Fe}_2\text{O}_3/\text{rGO}/\text{CNFs-20}$ should be attributed to its distinctive hierarchical structure. The addition of GO strengthens the mechanical flexibility of the film and induces the formation of amorphous $\text{am-Fe}_2\text{O}_3$ nanoparticles, which possess high capacitive storage and lower reaction activation energy compared with crystalline ones

(Fig. 6c) [19]. Without the lattice boundaries, the isotropic structure affords accessible transmission tunnels and storage sites for Li^+ ions, leading to faster reaction kinetics [42]. Moreover, the conductive CNFs with abundant cracks provide ideal channels for the electrolyte wetting, Li^+ ions diffusion, and electron transportation (Fig. 6d). With intensive connection to anchor the am- Fe_2O_3 active species, the CNFs matrix not only efficiently accommodate the volume changes of am- Fe_2O_3 , but also guarantees its robust structure and satisfactory reversible stability in extended cycling. In view of these fantastic structure and properties, flexible electrodes with superior electrochemical performance are deservedly achieved.

4. Conclusion

In summary, we have successfully developed novel button-shaped amorphous $\text{Fe}_2\text{O}_3/\text{rGO}/\text{carbon}$ nanofibers films through facile in-situ electrospinning and subsequent one-step carbonization. Intercalation of highly oxidized GO induces growth of button-shaped amorphous Fe_2O_3 nanoparticles located onto rimous CNFs matrix and simultaneously improves the mechanical flexibility of the resulting film. The amorphous nature enables Fe_2O_3 to achieve high capacitive storage, faster reaction kinetics, and excellent reversibility during electrochemical processes. The intimate connection between am- Fe_2O_3 and conductive carbon skeleton can facilitate electron transport, alleviate volume change, and enhance structural stability. Owing to the distinctive hierarchical structure, the am- $\text{Fe}_2\text{O}_3/\text{rGO}/\text{CNFs}$ -20 film delivers an excellent reversible capacity of 811 mA h g^{-1} at 0.1 A g^{-1} , as well as remarkable rate performance and cycling stability (584 mA h g^{-1} over 400 cycles at a high current density of 2 A g^{-1}). The electrode also exhibits satisfactory flexibility and great potential for application in flexible LIBs. We believe this work may open up a feasible avenue for the synthesis of amorphous TMOs based composites and designing of high-performance electrodes for flexible LIBs and beyond.

Acknowledgements

This work was financially supported by the National Natural Science Foundation of China (No. 51572296, U1662113, 51873231), China; the Fundamental Research Fund for the Central Universities (No. 18CX02015A, 15CX08005A), China; the CAS Key Laboratory of Carbon Materials (No. KLCMKFJJ1705), China; the Shandong Provincial Natural Science Foundation (No. ZR2016BB18), China; the Shandong Provincial Natural Science Foundation (ZR2018ZC1458), China; the Financial Support from Taishan Scholar Project (No. ts201712020) and Technological Leading Scholar of 10000 Talent Project (No. W03020508), China.

Appendix A. Supplementary data

Supplementary data to this article can be found online at <https://doi.org/10.1016/j.cej.2019.03.076>.

References

- [1] K. Fu, J. Cheng, T. Li, L. Hu, Flexible batteries: from mechanics to devices, *ACS Energy Lett.* 1 (2016) 1065–1079.
- [2] Y. Tang, Y. Zhang, W. Li, B. Ma, X. Chen, Rational material design for ultrafast rechargeable lithium-ion batteries, *Chem. Soc. Rev.* 44 (2015) 5926–5940.
- [3] Z. Pan, J. Ren, G. Guan, X. Fang, B. Wang, S. Doo, I. Son, X. Huang, H. Peng, Synthesizing nitrogen-doped core-sheath carbon nanotube films for flexible lithium ion batteries, *Adv. Energy Mater.* 6 (2016) 1600271.
- [4] G. Zhou, F. Li, H. Cheng, Progress in flexible lithium batteries and future prospects, *Energy Environ. Sci.* 7 (2014) 1307–1338.
- [5] G. Qian, B. Zhu, X. Liao, H. Zhai, A. Srinivasan, N.J. Fritz, Q. Cheng, M. Ning, B. Qie, Y. Li, S. Yuan, J. Zhu, X. Chen, Y. Yang, Bioinspired, spine-like, flexible, rechargeable lithium-ion batteries with high energy density, *Adv. Mater.* 30 (2018) 1704947.
- [6] W. Qi, J. Shapter, Q. Wu, T. Yin, G. Gao, D. Cui, Nanostructured anode materials for lithium-ion batteries: principle, recent progress and future perspectives, *J. Mater. Chem. A* 5 (2017) 19521–19540.
- [7] R. Liu, C. Shen, C. Zhang, J. Iocozzia, Q. Wang, S. Zhao, K. Yuan, Z. Lin, Hierarchical bicomponent TiO_2 hollow spheres as a new high-capacity anode material for lithium-ion batteries, *J. Mater. Sci.* 53 (2018) 8499–8509.
- [8] R. Liu, W. Su, C. Shen, J. Iocozzia, S. Zhao, K. Yuan, N. Zhang, C. Wang, Z. Lin, Hydrothermal synthesis of hollow SnO_2 spheres with excellent electrochemical performance for anodes in lithium ion batteries, *Mater. Res. Bull.* 96 (2017) 443–448.
- [9] S. Yoon, S. Lee, S. Kim, K. Park, D. Cho, Y. Jeong, Carbon nanotube film anodes for flexible lithium ion batteries, *J. Power Sources* 279 (2015) 495–501.
- [10] L. Huang, Q. Guan, J. Cheng, C. Li, W. Ni, Z. Wang, Y. Zhang, B. Wang, Free-standing N-doped carbon nanofibers/carbon nanotubes hybrid film for flexible, robust half and full lithium-ion batteries, *Chem. Eng. J.* 334 (2018) 682–690.
- [11] Y. He, B. Matthews, J. Wang, L. Song, X. Wang, G. Wu, Innovation and challenges in materials design for flexible rechargeable batteries: from 1D to 3D, *J. Mater. Chem. A* 6 (2018) 735–753.
- [12] J. Ji, Y. Li, W. Peng, G. Zhang, F. Zhang, X. Fan, Advanced graphene-based binder-free electrodes for high-performance energy storage, *Adv. Mater.* 27 (2015) 5264–5279.
- [13] S. Li, Y. Zhao, Z. Liu, L. Yang, J. Zhang, M. Wang, R. Che, Flexible graphene-wrapped carbon nanotube/graphene/ MnO_2 3D multilevel porous film for high-performance lithium-ion batteries, *Small* 14 (2018) 1704947.
- [14] J. Ren, R. Ren, Y. Lv, A flexible 3D graphene/CNT/ MoS_2 hybrid foam anode for high-performance lithium-ion battery, *Chem. Eng. J.* 353 (2018) 419–424.
- [15] M. Balogun, Z. Wu, Y. Luo, W. Qiu, X. Fan, B. Long, M. Huang, P. Liu, Y. Tong, High power density nitridated hematite ($\alpha\text{-Fe}_2\text{O}_3$) nanorods as anode for high-performance flexible lithium ion batteries, *J. Power Sources* 308 (2016) 7–17.
- [16] T.R. Penki, S. Shivakumara, M. Minakshi, N. Munichandraiah, Porous flower-like $\alpha\text{-Fe}_2\text{O}_3$ nanostructure: a high performance anode material for lithium-ion batteries, *Electrochim. Acta* 167 (2015) 330–339.
- [17] M. Zheng, H. Tang, L. Li, Q. Hu, L. Zhang, H. Xue, H. Pang, Hierarchically nanostructured transition metal oxides for lithium-ion batteries, *Adv. Sci.* 5 (2018) 1700592.
- [18] L. Xia, S. Wang, G. Liu, L. Ding, D. Li, H. Wang, S. Qiao, Flexible SnO_2/N -Doped carbon nanofiber films as integrated electrodes for lithium-ion batteries with superior rate capacity and long cycle life, *Small* 12 (2016) 853–859.
- [19] Q. Wu, R. Zhao, X. Zhang, W. Li, R. Xu, G. Diao, M. Chen, Synthesis of flexible $\text{Fe}_3\text{O}_4/\text{C}$ nanofibers with buffering volume expansion performance and their application in lithium-ion batteries, *J. Power Sources* 359 (2017) 7–16.
- [20] W. Xiong, Y. Jiang, Y. Xia, Y. Qi, W. Sun, C. Hu, R. He, B. Chen, Y. Liu, X. Zhao, A sustainable approach for scalable production of $\alpha\text{-Fe}_2\text{O}_3$ nanocrystals with 3D interconnected porous architectures on flexible carbon textiles as integrated electrodes for lithium-ion batteries, *J. Power Sources* 401 (2018) 65–72.
- [21] H. Cha, J. Kim, Y. Lee, J. Cho, M. Park, Issues and challenges facing flexible lithium-ion batteries for practical application, *Small* 14 (2018) 1702989.
- [22] S. Yan, K. Abhilash, L. Tang, M. Yang, Y. Ma, Q. Xia, Q. Guo, H. Xia, Research advances of amorphous metal oxides in electrochemical energy storage and conversion, *Small* 15 (2019) 1804371.
- [23] S. Oh, I. Kim, K. Adpakpang, S. Hwang, The beneficial effect of nanocrystalline and amorphous nature on the anode performance of manganese oxide for lithium ion batteries, *Electrochim. Acta* 174 (2015) 391–399.
- [24] Z. Wei, D. Wang, X. Yang, C. Wang, G. Chen, F. Du, From crystalline to amorphous: an effective avenue to engineer high-performance electrode materials for sodium-ion batteries, *Adv. Mater. Inter.* 5 (2018) 1800639.
- [25] L. Shi, Y. Li, F. Zeng, S. Ran, C. Dong, S. Leu, S.T. Boles, K.H. Lam, In situ growth of amorphous Fe_2O_3 on 3D interconnected nitrogen-doped carbon nanofibers as high-performance anode materials for sodium-ion batteries, *Chem. Eng. J.* 356 (2019) 107–116.
- [26] M. Xie, X. Sun, H. Sun, T. Porcelli, S.M. George, Y. Zhou, J. Lian, Stabilizing an amorphous $\text{V}_2\text{O}_5/\text{carbon}$ nanotube paper electrode with conformal TiO_2 coating by atomic layer deposition for lithium ion batteries, *J. Mater. Chem. A* 4 (2016) 537–544.
- [27] X. Zhu, X. Jiang, X. Chen, X. Liu, L. Xiao, Y. Cao, Fe_2O_3 Amorphous nanoparticles/graphene composite as high-performance anode materials for lithium-ion batteries, *J. Alloy. Compd.* 711 (2017) 15–21.
- [28] Y. Huang, Z. Lin, M. Zheng, T. Wang, J. Yang, F. Yuan, X. Lu, L. Liu, D. Sun, Amorphous Fe_2O_3 nanoshells coated on carbonized bacterial cellulose nanofibers as a flexible anode for high-performance lithium ion batteries, *J. Power Sources* 307 (2016) 649–656.
- [29] K. Zhu, X. Wang, J. Liu, S. Li, H. Wang, L. Yang, S. Liu, T. Xie, Novel amorphous $\text{MoS}_2/\text{MoO}_3$ /nitrogen-doped carbon composite with excellent electrochemical performance for lithium ion batteries and sodium ion batteries, *ACS Sustain. Chem. Eng.* 5 (2017) 8025–8034.
- [30] Y. Kobayashi, J. Abe, K. Kawase, K. Takahashi, B.D. Vogt, S. Shiratori, Enhanced stability of smoothly electrodeposited amorphous Fe_2O_3 at electrospun carbon nanofibers as self-standing anodes for lithium ion batteries, *New J. Chem.* 42 (2018) 1867–1878.
- [31] D. Marciano, D. Kosynkin, J. Berlin, A. Sinitskii, Z. Sun, A. Slesarev, L.B. Alemay, W. Lu, J.M. Tour, Improved synthesis of graphene oxide, *ACS Nano* 4 (2010) 4806–4814.
- [32] Q. Zhao, J. Liu, Y. Wang, W. Tian, J. Liu, J. Zang, H. Ning, C. Yang, M. Wu, Novel In-situ redox synthesis of $\text{Fe}_3\text{O}_4/\text{rGO}$ composites with superior electrochemical performance for lithium-ion batteries, *Electrochim. Acta* 262 (2018) 233–240.
- [33] H. Huang, X. Wang, E. Tervoort, G. Zeng, T. Liu, X. Chen, A. Sologubenko, M. Niederberger, Nano-sized structurally disordered metal oxide composite aerogels as high-power anodes in hybrid supercapacitors, *ACS Nano* 12 (2018)

- 2753–2763.
- [34] J. He, S. Zhao, Y. Lian, M. Zhou, L. Wang, B. Ding, S. Cui, Graphene-doped carbon/ Fe_3O_4 porous nanofibers with hierarchical band construction as high-performance anodes for lithium-ion batteries, *Electrochim. Acta* 229 (2017) 306–315.
- [35] A. Ferrari, J. Meyer, V. Scardaci, C. Casiraghi, M. Lazzeri, F. Mauri, S. Piscanec, D. Jiang, K. Novoselov, S. Roth, Raman spectrum of graphene and graphene layers, *Phys. Rev. Lett.* 97 (2006) 187401.
- [36] M. Mukadam, S. Yusuf, P. Sharma, S. Kulshreshtha, Magnetic behavior of field induced spin-clusters in amorphous Fe_2O_3 , *J. Magn. Magn. Mater.* 269 (2004) 317–326.
- [37] L. Machala, R. Zboril, A. Gedanken, Amorphous iron(III) oxide-A review, *J. Phys. Chem. B* 111 (2007) 4003–4018.
- [38] F. Wang, Y. Zhu, W. Tian, X. Lv, H. Zhang, Z. Hu, Y. Zhang, J. Ji, W. Jiang, Co-doped Ni_3S_2 @CNT arrays anchored on graphite foam with a hierarchical conductive network for high-performance supercapacitors and hydrogen evolution electrodes, *J. Mater. Chem. A* 6 (2018) 10490–10496.
- [39] B. Jiang, Y. He, B. Li, S. Zhao, S. Wang, Y. He, Z. Lin, Polymer-templated formation of polydopamine-coated SnO_2 nanocrystals: anodes for cyclable lithium-ion batteries, *Angew. Chem. Int. Ed.* 56 (2017) 1869–1872.
- [40] Z. Zheng, Y. Zao, Q. Zhang, Y. Cheng, H. Chen, K. Zhang, M. Wang, D. Peng, Robust erythrocyte-Like Fe_2O_3 @carbon with yolk-shell structures as high-performance anode for lithium ion batteries, *Chem. Eng. J.* 347 (2018) 563–573.
- [41] X. Fan, W. Peng, Y. Li, X. Li, S. Wang, G. Zhang, F. Zhang, Deoxygenation of exfoliated graphite oxide under alkaline conditions: a green route to graphene preparation, *Adv. Mater.* 20 (2008) 4490–4493.
- [42] D. Li, J. Zhou, X. Chen, H. Song, Amorphous Fe_2O_3 /graphene composite nanosheets with enhanced electrochemical performance for sodium-ion battery, *ACS Appl. Mater. Inter.* 8 (2016) 30899–30907.
- [43] W. Li, F. Yang, Y. Rui, B. Tang, Strong covalent interaction Fe_2O_3 /nitrogen-doped porous carbon fiber hybrids as free-standing anodes for lithium-ion batteries, *J. Mater. Sci.* 54 (2019) 6500–6514.
- [44] J. Zhang, A. Yu, Nanostructured transition metal oxides as advanced anodes for lithium-ion batteries, *Sci. Bull.* 60 (2015) 823–838.
- [45] Z. Li, Y. Mao, Q. Tian, W. Zhang, L. Yang, Extremely facile preparation of high-performance Fe_2O_3 anode for lithium-ion batteries, *J. Alloy. Compd.* 784 (2019) 125–133.
- [46] S. Jin, H. Deng, D. Long, X. Liu, L. Zhan, X. Liang, W. Qiao, L. Ling, Facile synthesis of hierarchically structured Fe_3O_4 /carbon micro-flowers and their application to lithium-ion battery anodes, *J. Power Sources* 196 (2011) 3887–3893.
- [47] J. Guo, H. Zhu, Y. Sun, L. Tang, X. Zhang, Pie-like free-standing paper of graphene paper/ Fe_3O_4 nanorod Array@Carbon as integrated anode for robust lithium storage, *Chem. Eng. J.* 309 (2017) 272–277.
- [48] X. Zhu, X. Song, X. Ma, G. Ning, Enhanced electrode performance of Fe_2O_3 nanoparticle-decorated nanomesh graphene as anodes for lithium-ion batteries, *ACS Appl. Mater. Inter.* 6 (2014) 7189–7197.
- [49] L. Yin, Y. Gao, I. Jeon, H. Yang, J. Kim, S.Y. Jeong, C.R. Cho, Rice-panicle-like gamma- Fe_2O_3 @C nanofibers as high-rate anodes for superior lithium-ion batteries, *Chem. Eng. J.* 356 (2019) 60–68.
- [50] X. Lv, Y. Zhu, T. Yang, H. Zhang, X. Cui, H. Yue, D. Liu, J. Chen, J. Ji, Liquid-Solid-solution assembly of morphology-controllable Fe_2O_3 /graphene nanostructures as high-performance LIB anodes, *Ceram. Int.* 42 (2016) 19006–19011.
- [51] S. Park, G. Park, Y. Kang, Three-dimensional porous microspheres comprising hollow Fe_2O_3 nanorods/CNT building blocks with superior electrochemical performance for lithium ion batteries, *Nanoscale* 10 (2018) 11150–11157.
- [52] Y. Jiang, D. Zhang, Y. Li, T. Yuan, N. Bahlawane, C. Liang, W. Sun, Y. Lu, M. Yan, Amorphous Fe_2O_3 as a high-capacity, high-rate and long-life anode material for lithium ion batteries, *Nano Energy* 4 (2014) 23–30.
- [53] J. Guo, Q. Liu, C. Wang, M. Zachariah, Interdispersed amorphous MnO_x -carbon nanocomposites with superior electrochemical performance as lithium-storage material, *Adv. Funct. Mater.* 22 (2012) 803–811.
- [54] S. Yu, V.M.H. Ng, F. Wang, Z. Xiao, C. Li, L. Kong, W. Que, K. Zhou, Synthesis and application of iron-based nanomaterials as anodes of lithium-ion batteries and supercapacitors, *J. Mater. Chem. A* 6 (2018) 9332–9367.
- [55] T. Jiang, F. Bu, X. Feng, I. Shakir, G. Hao, Y. Xu, Porous Fe_2O_3 nanoframeworks encapsulated within three-dimensional graphene as high-performance flexible anode for lithium-ion battery, *ACS Nano* 11 (2017) 5140–5147.
- [56] R. Liu, C. Zhang, Q. Wang, C. Shen, Y. Wang, Y. Dong, N. Zhang, M. Wu, Facile synthesis of alpha- Fe_2O_3 @C hollow spheres as ultra-long cycle performance anode materials for lithium ion battery, *J. Alloy. Compd.* 742 (2018) 490–496.